JACS
JOURNAL OF THE AMERICAN CHEMICAL SOCIETY

Article

pubs.acs.org/JACS

Branched Artificial Nanofinger Arrays by Mesoporous Interfacial Atomic Rearrangement

Biao Kong,[†,‡] Jing Tang,[†] Yueyu Zhang,[§] Cordelia Selomulya,[‡] Xingao Gong,[§] Yang Liu,[†] Wei Zhang,[†] Jianping Yang,[†] Wenshuo Wang,[#] Xiaotian Sun,[#] Yufei Wang,[⊥] Gengfeng Zheng,*[,†] and Dongyuan Zhao*[,†,‡]

[†]Department of Chemistry, Laboratory of Advanced Materials, Collaborative Innovation Center of Chemistry for Energy Materials, Shanghai Key Laboratory of Molecular Catalysis and Innovative Materials, [§]Key Laboratory of Computational Physical Sciences, Ministry of Education, State Key Laboratory of Surface Physics, and Department of Physics, and [#]Department of Cardiovascular Surgery, Zhongshan Hospital, Fudan University, Shanghai 200433, P. R. China

[‡]Department of Chemical Engineering and [⊥]Department of Materials Engineering, Monash University, Wellington Road, Clayton, Victoria 3800, Australia

Supporting Information

ABSTRACT: The direct production of branched semiconductor arrays with highly ordered orientation has proven to be a considerable challenge over the last two decades. Here we report a mesoporous interfacial atomic rearrangement (MIAR) method to directly produce highly crystalline, finger-like branched iron oxide nanoarrays from the mesoporous nanopyramids. This method has excellent versatility and flexibility for heteroatom doping of metallic elements, including Sn, Bi, Mn, Fe, Co, Ni, Cu, Zn, and W, in which the mesoporous nanopyramids first absorb guest-doping molecules into the mesoporous channels and then convert the mesoporous pyramids into branching artificial nanofingers. The crystalline structure can provide more optoelectronic active sites of the nanofingers by interfacial atomic rearrangements of doping molecules and mesopore channels at the porous solid−solid interface. As a proof-of-concept, the Sn-doped Fe_2O_3 artificial nanofingers (ANFs) exhibit a high photocurrent density of ∼1.26 mA/cm^2, ∼5.25-fold of the pristine mesoporous Fe_2O_3 nanopyramid arrays. Furthermore, with surface chemical functionalization, the Sn-doped ANF biointerfaces allow nanomolar level recognition of metabolism-related biomolecules (∼5 nm for glutathione). This MIAR method suggests a new growth means of branched mesostructures, with enhanced optoelectronic applications.

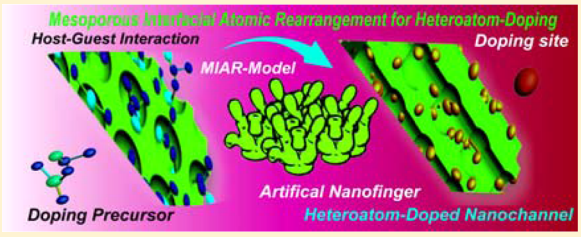

1. INTRODUCTION

The stretching of one-dimensional (1D) human fingers and the separation of individual fingers provide directional outreach and large surface area for sensing changes in the external environment.[1] Thus, material structures that mimic human fingers can be substantially beneficial for effective light harvesting and charge transport, while at the same time can provide a large interface for surface chemical reactions, in an analogy to the stretching and extending of green plants for sunlight-based photosynthesis.[2] Over the past two decades, micro/nanomaterial arrays with a desired morphology, such as nanowire,[3,4] nanotube,[5,6] nanoribbon,[7−9] nanocone,[10−12] nanoantenna,[13] nanorod/nanopillar,[14,15] nanopore,[16−18] nanodome,[19] nanopyramid,[20] and nanoantenna[21,22] arrays, have drawn much attention as their extraordinary optoelectronic properties.[23] To date, branched nanostructures fabricated by different top-down and bottom-up methods, such as metal-catalyzed vapor−liquid−solid (VLS) growth,[24−28] screw dislocation driven growth,[29−31] and zinc-blende/wurtzite stacking faults,[32,33] represent similar advantages to the finger structures. Nonetheless, the crystalline of branches often leads to different orientations of individual branches,[29,30] thus limiting their signal collection efficiency. The controlled oriented growth and doping of these nanostructures offer direct electrical pathways for photogenerated electrons and increase their transport rate to improve the optoelectric performance.[34,35] To date, the realization of bent and stretched finger-like nanoarrays, with preferred orientation, controlled heteroatom doping, and facile synthetic capability, has remained a considerable challenge.[2,34] Here we demonstrate an artificial nanofinger (ANF) semiconductor produced directly from highly oriented mesoporous iron oxide pyramid arrays, via a mesoporous interfacial atomic rearrangement (MIAR) process. Prussian blue pyramid arrays are first synthesized by an interfacial hydrolysis and assembly, followed by thermal annealing to decompose into mesoporous iron oxide pyramid arrays with high orientation.[20] Then the mesoporous nanopyramids first absorb guest-doping molecules into the mesoporous channels and convert the mesoporous pyramids

Received: February 16, 2015
Published: March 12, 2015

DOI: 10.1021/jacs.5b01747
J. Am. Chem. Soc. 2015, 137, 4260−4266

into heteroatom-doped branching artificial nanofingers by further annealing, leading to the formation of oriented, finger-like structures with single-crystallinity and joints. This route has excellent versatility and flexibility for heteroatom-doping of metallic elements, including Sn, Bi, Mn, Fe, Co, Ni, Cu, Zn, and W. The crystalline structure can provide more optoelectronic active sites of the nanofingers by interfacial atomic rearrangements of doping guest molecules and mesopore channels at the porous solid−solid interface. As a proof of concept, the Sn-doped Fe_2O_3 ANFs exhibit the high photocurrent density of ~1.26 mA/cm^2 at 0.23 V vs Ag/AgCl, which is ~5.25 and 2.07-fold of the pristine pyramids and pristine undoped Fe_2O_3 ANFs, respectively. Moreover, Sn-doped Fe_2O_3 ANF−hemin heterointerface allows for unprecedented nanomolar level (~5 nm, limit of detection) of capturing and recognition for glutathione (GSH) that have not yet been demonstrated with the traditional biointerfaces. This method enables the formation of branching structures of the materials or heteroatom-doped structures from mesopore nanoarrays. This approach adds to the branching structure synthesis toolbox, creating structures from the interfacial atomic rearrangement paradigm that are previously impossible to achieve from traditional approaches.

2. RESULTS AND DISCUSSION

2.1. Fabrication of Heteroatom-Doped Artificial Nanofingers (ANFs). In brief, Prussian blue pyramids with cubic α-Po type network topology[35] are first grown on a flexible titanium foil and then converted into mesoporous pyramids through an interfacial pyrolysis process (Figures 1a and S1).[20] The color of the Ti film substrates changes from silver white to deep blue after the synthesis, implying that Prussian blue is grown on the surface (Figure S2). Scanning electron microscopy (SEM) images (Figure 1b,c) show that the Ti growth substrate is covered by a thin layer of oriented Prussian blue pyramids, with a thickness of ~150 nm (Figure S3). The average bottom size of the as-grown pyramids is ~150 nm, with a preferred (100) crystal orientation. This is attributed to the fastest growth rate along ⟨100⟩ direction that drives the strongly preferred crystal orientation.[20] High-resolution transmission electron microscopy (HRTEM) images show that each Prussian blue nanopyramid is crystalline (Figure S4). These Prussian blue nanopyramid films exhibit excellent flexibility and stable morphology for over 200 times of bending and releasing, without observable deformation (Figure S5). After pyrolysis, the color of the pyramids film changes from blue to dark red, implying the formation of iron oxides (Figure S6). The structural model (Figure 1d) and SEM images (Figure 1e) exhibit a discontinuous mesoporous nanopyramid film, with island-like aggregation and separation in a size of ~5 × 5 μm. Mesopores can be clearly observed on each of the nanopyramids (Figure 1f). HRTEM images and the corresponding selected area electron diffraction (SAED) pattern show that each nanopyramid is constructed by poly crystalline iron oxide frameworks with ~15 nm mesopores (Figure S7). N_2 sorption isotherms show that the mesoporous iron oxide nanopyramid arrays have a high surface area of ~165 m^2 g^{-1} and a large mean pore size of ~20 nm (Figure S8). X-ray photoelectron spectroscopy (XPS) analysis of the nanopyramid array films demonstrates one main peak around 533 eV and two others at ~725 and 710 eV (Figure S9), corresponding to O_{1s}, Fe $2p_{1/2}$, and $2p_{3/2}$ in Fe_2O_3, respectively, confirming that all films are mainly composed of Fe_2O_3 from pyrolysis.[20,35]

The mesoporous Fe_2O_3 nanopyramids can be further converted into nanofingers by controlled interfacial pyrolysis, during the guest molecules of doping sources can be readily adsorbed and converted to tune the surface area[36] and porosity.[37] As a proof of concept, Sn-doped ANFs (Sn-ANFs) are grown on Ti substrates over a range of the guest molecule ($SnCl_2$) to host (mesoporous pyramids) ratios. The typical doping ratio between Sn and Fe is 5% (atomic ratio). The structural model (Figure 1g) and SEM images (Figure 1h, (i) shows interconnected finger-like morphologies with a diameter of 20 nm (Figure 2a) (the sizes vary with the growth conditions). The corresponding SAED pattern (Figure 2b) and HRTEM image (Figure 2c) reveal the single crystalline nature of a Sn-ANF. In addition, the HRTEM image and corresponding SAED pattern (Figure 2d and insets) of a joint of two ANFs display single crystalline nature. The elemental mappings of representative Sn-ANFs show uniform distribution of the Fe and Sn signals over the entire ANFs

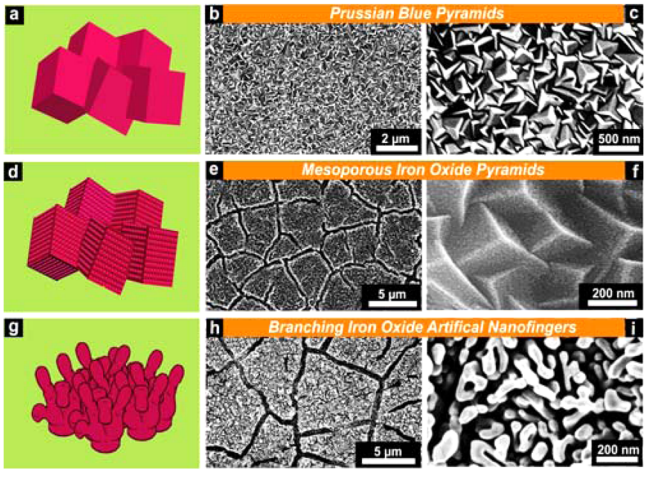

Figure 1. Branching artificial nanofingers derived from mesoporous pyramids. (a−c) Structural model (a), top-view SEM image (b), and enlarged SEM image (c) of the obtained Prussian blue pyramids. Prussian blue pyramids were grown on a flexible titanium foil by a structure-directing surfactant-free hydrolysis and assembly. (d−f) Prussian blue pyramids as viewed perpendicularly to ⟨100⟩. Structural model (d), top-view SEM image (e), and enlarged SEM image (f) of the mesoporous iron oxide pyramids from an interfacial thermal pyrolysis. (g−i) Structural model (g), top-view SEM image (h), and enlarged SEM image (i) of the Sn-doped branching iron oxide artificial nanofingers derived from mesoporous pyramids.

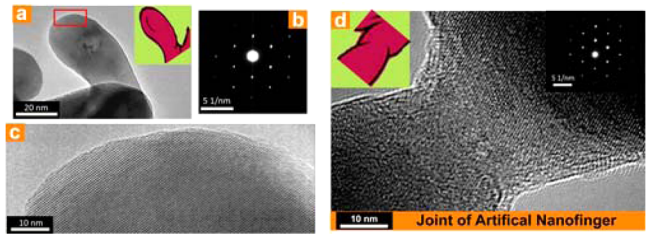

Figure 2. Structural analysis. (a−c) The TEM image (a), enlarged TEM image (b), and corresponding SAED pattern (c) of one nanofinger. (d) The enlarged TEM image and corresponding SAED pattern (inset) of one joint of the artificial nanofinger. All the microstructural analyses indicate the unique nature of the complete crystallization of the artificial nanofingers.

DOI: 10.1021/jacs.5b01747
J. Am. Chem. Soc. 2015, 137, 4260−4266

(Figure S10), suggesting successful Sn doping over the ANFs. The EDX spectra (Figure S11), XRD patterns (Figure S12), XPS spectra (Figure S13), and HRTEM images (Figure 2) all clearly show that Sn is doped over the entire ANFs. The Sn-doping concentration ranges from 0.1 ± 0.03 to 13.5 ± 2.5 mol % at different adsorption condition via a quantitative analysis of inductively coupled plasma mass spectrometry (ICP-MS) following acid digestion (Figures S14 and S15, Table S1).

2.2. Optoelectronic Properties and Performance. The Sn-doped Fe_2O_3 ANFs are then fabricated as photoanodes for optoelectronic property studies (Figure 3a). For comparison,

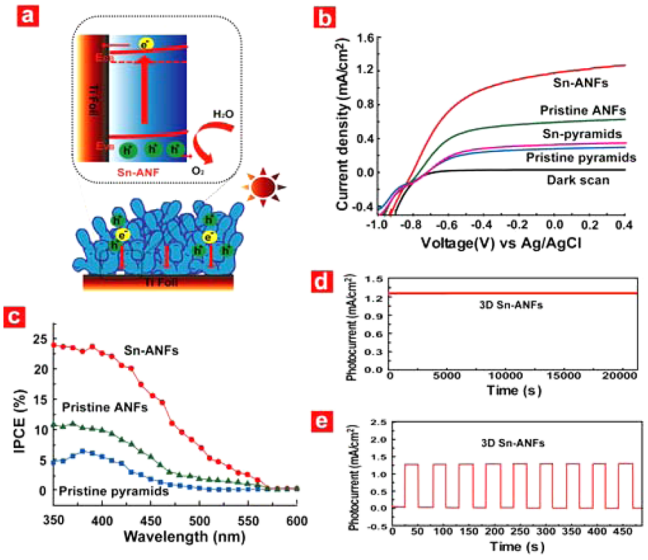

Figure 3. Optoelectronic performance. (a) Schematic energy diagram of the branching artificial nanofinger-based photoelectrochemical interface. (b) Line sweep voltammograms of the pristine pyramids, Sn-doped pyramids, pristine ANFs, and Sn-doped ANFs. The dark current of the Sn-doped ANFs is also plotted for comparison. (c) IPCE curves of the pristine pyramids, the pristine ANFs, and the Sn-doped ANFs. (d) Time-dependent photocurrent density of the Sn-doped ANFs photoanode under a continuous simulated sunlight illumination. (e) Time-dependent photocurrent density of the Sn-doped ANFs photoanode at repeated on/off cycles of simulated sunlight illumination.

the pristine mesoporous Fe_2O_3 nanopyramids and undoped mesoporous Fe_2O_3 ANFs were also prepared as photoanodes and measured under similar conditions (Experimental Section). Under air mass 1.5 global (AM 1.5G) simulated solar light illumination, the photocurrent density of the pristine mesoporous Fe_2O_3 nanopyramids is measured to be ~0.24 mA/cm^2 at 0.23 V vs Ag/AgCl (Figure 3b, blue curve). A clear increase of the photocurrent is observed from the pristine ANFs, ~0.61 mA/cm^2 at 0.23 V vs Ag/AgCl (Figure 3b, green curve), indicating the crystallinity effect on the photoactivity of ANFs, in good accord with the result of undoped hematite reported.[20,38] Remarkably, the Sn-doped ANFs exhibit the highest photocurrent density among these three photoanodes (Figure 3b, red curve, Figure S16), which reaches ~1.26 mA/cm^2 at 0.23 V vs Ag/AgCl and is ~5.25-fold of the pristine mesoporous Fe_2O_3 nanopyramids, which is the reported highest enhancement of optoelectronic performance by heteroatom-doping (Table S2). No significant enhancement of photocurrent density is observed for the Sn-doped nanopyramids as a control (Figure 3b, pink curve). The incident photo-to-current conversion efficiency (IPCE) is further measured at −0.2 V vs Ag/AgCl from 350 to 600 nm for evaluating the external quantum efficiency of these photoanodes (Figure 3c). The signal responses of all pristine photoanodes are mainly located in the wavelength region of 350−570 nm and decrease to almost zero for wavelengths above 580 nm.[20] Compared to the pristine mesoporous Fe_2O_3 nanopyramids between 3 and 7% (Figure 3c, blue curve), the IPCE value of the pristine ANFs (Figure 3c, green curve) is increased to 4−12%, indicating a higher efficiency in the conversion. The Sn-doped Fe_2O_3 ANFs (Figure 3c, red curve) demonstrate the highest IPCE value of ~10−25% in the region of 300−500 nm. Moreover, the time-dependent photocurrent measurement of the Sn-doped Fe_2O_3 ANFs displays a highly stable photocurrent density of ~1.26 mA/cm^2 at 0.23 V vs Ag/AgCl under continuous solar illumination for 20,000 s without observable degradation (Figure 3d), as well as a clear correlation with on/off cycles of simulated solar light (Figure 3e).

2.3. ANF-Based Optoelectronic Nanobiointerface. The bioinspired nanofingers can substantially benefit for effective light harvesting and charge transport, while at the same time provide more active sites for surface chemical reactions. Thus, incorporating nanostructures and extracellular redox biomolecules allows for excellent biocompatibility and more active components.[22,39] As a proof of concept, a Sn−ANF−hemin heterointerface by engineering a mimic enzyme, hemin, is carried out to evaluate the potential for signal capturing and recognition of a biomolecule model, glutathione (GSH) (Figure 4a). GSH serves many important cellular functions, including intracellular signal transduction, xenobiotic metabolism, and gene regulation.[40] Real-time and long-term

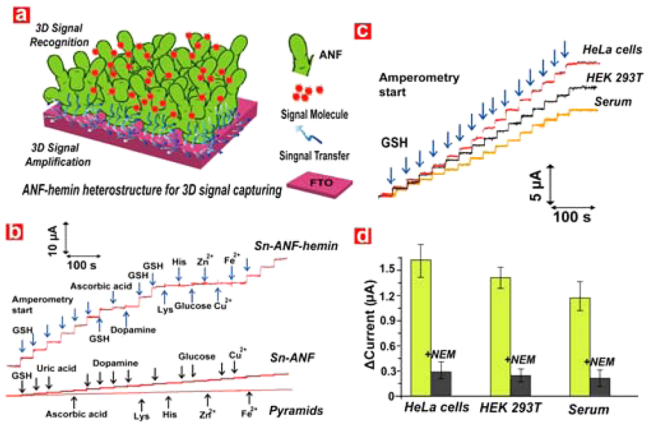

Figure 4. Optoelectronic biomolecule recording. (a) Proposed strategy of 3D signal capturing, recognition, and amplification based on the ANF−hemin heterointerfaces. (b) Current versus time curves of a Sn-ANF nanobiointerface for successive addition of GSH (10 nM) to PBS solution (pH 7.4) at 0.2 V under 100 mW/cm^2 simulated sunlight illumination, showing the excellent selectivity toward GSH. For comparison, the pristine Sn-ANFs do not show signals to the addition of GSH. (c) Current versus time data of a Sn-ANF nanobiointerface for extracts from solutions of Hela cells, HEK 293T cells, and serum with 1:200 dilution in PBS. (d) Cellular assay and GSH detection in Hela cell, HEK 293T cell, and serum extracts. Conditions are presented for each column: pristine HeLa cell extracts, mixture of HeLa cell extracts and NEM, pristine HEK 293T cell extracts, mixture of HeLa cell extracts and NEM serum containing GSH, and serum containing both GSH and NEM.

DOI: 10.1021/jacs.5b01747
J. Am. Chem. Soc. 2015, 137, 4260−4266

monitoring of GSH in biological samples is commonly considered as an extremely challenging task, as GSH is easily destroyed in the presence of O_2, especially at ultralow concentration (nanomolar level) measurements.[41] The strategy to construct the Sn−ANF−hemin heterobiointerface for *in situ* culture of living cells and signal capturing and recognition are shown in Figure S17. The sensor amperogram of the hemin-functionalized Fe_2O_3 ANFs is obtained by measuring the time-dependent photocurrent changes upon successive injections of GSH solution (10 nM), with a 0.2 V bias to minimize the interference of other reductive species coexisting in the samples (Figure 4b). The photogenerated electrons in hemin can transfer to the conduction band of 3D hematite ANF. At the same time, hemin can specifically recognize the presence of trace GSH, which acts as the acceptors of photogenerated holes in hemin, which are subsequently transferred to the Ti thin film current collector, leading to a signal increase of the photocurrent (Figure S18).[40−43] The hemin-functionalized Sn-doped Fe_2O_3 ANFs respond quickly and reach equilibrium within 10 s upon each injection of GSH, with the detection limit of GSH as ∼5 nM, which is the lowest among all the detection methods reported previously (Table S3). In contrast, hemin-functionalized pristine Fe_2O_3 ANFs show a weak signal toward the GSH addition, while the Fe_2O_3 pyramids obtain a negligible response (Figure 4b). The selectivity is demonstrated by measuring the response for other metal ions, amino acids, and common chemical/biological interferences, such as uric acid, ascorbic acid, dopamine, histidine, lysine, glucose, glutamine, valine, Zn^{2+}, Cu^{2+}, and Fe^{2+}, showing a negligible or much smaller signal response than GSH (Figure 4b, Figure S19a). In further tests of the Sn−ANF−hemin heterobiointerface, over 90% of the initial signal response is maintained for over 50 days, suggesting excellent stability and reproducibility for the biointerface sensing (Figure S19b). Furthermore, no significant signal changes and lattice changes are found during the adding of different cations (Na^+, K^+, Zn^{2+}, Cu^{2+}, Ca^{2+}, Fe^{2+}, and Mg^{2+}) into solution (Figure S20).

The performance of the Sn-doped Fe_2O_3 ANFs is further investigated by measuring different living cells, including HeLa cells (cancer cell line) and human embryonic kidney (HEK) 293T cells (normal cell line) (∼10^2 to 10^6 cells/mL). The Sn-doped Fe_2O_3 ANFs show a sensitive amperometric response after the injection of cell extracts, with a detection limit of ∼6000 and ∼4000 cells/mL for HeLa cells and HEK 293T cells, respectively (Figure 4c). Finally, the delivery of GSH in mouse serum (with 1:200 dilution in PBS) to the hemin-functionalized Sn-doped Fe_2O_3 ANFs leads to photocurrent signals at each injection, with the lowest detectable concentration of ∼15 nM (Figure 4c), suggesting the potential of direct recording of GSH from complex body fluids. The introduction of *N*-ethylmaleimide (NEM), a well-known thiol-blocking agent that can selectively decompose GSH,[42,43] into both the cell extracts and the GSH-containing serum, reduces the signal change to the background level (Figure 4d). This indicates that the signal increase at the nanobiointerface is attributed to the GSH produced inside these cells.

2.4. Doping and Morphology of Fe_2O_3 ANFs. The Sn-doping approach into the Fe_2O_3 ANFs can be broadly applied to a variety of metal dopants via the aforementioned host−guest chemistry. Metal dopants, including Bi, Mn, Fe, Co, Ni, Cu, Zn, and W under similar reaction conditions, have been demonstrated for controlled doping into the Fe_2O_3 ANFs, confirmed by EDX spectra (Figures S21a−S28a), XRD patterns (Figures S21b−S28b), XPS spectra (Figures S21c−S28c), and SEM images (Figure S29). This dopant incorporation allows for homogeneous dopant distribution and almost identical morphology and crystallinity compared to the undoped ANFs, with higher charge carrier mobility and visible-light absorbance.

To further investigate the formation mechanism of the Fe_2O_3 ANFs, control experiments using monodispersed Prussian blue nanocubes as precursors were conducted. The transformations of mesoscopic structure from Prussian blue nanocubes, to porous Fe_2O_3 nanocubes, and finally to porous rod-assembled nanocubes are observed. The Prussian blue nanocubes (Figure S30a,b) are found to convert into mesoporous nanocubes with partially interconnected pores at 450 °C (Figure S30c,d), and finally become rod-assembled nanocubes with a further increase of annealing temperature to 550 °C (Figure S30e,f). No branching artificial nanofingers are found during the whole process. In contrast, under the same annealing condition, the formation of the mesoporous pyramids to nanofingers is realized. By increasing temperature from room temperature to 450 and then 550 °C, the original Prussian blue nanopyramids are converted into mesoporous Fe_2O_3 nanopyramids and then into Fe_2O_3 ANFs. This morphology conversion process can be visualized by heating up the samples through consecutive steps, which shows an interface-migration process. With an increase of annealing temperature from 350 to 390 °C, a Sn-dopant precursor loaded mesoporous nanopyramid array with relative smaller mesopores (∼15 nm) (Figure S31a) is grown into relative large mesopores (∼25 nm) (Figure S31b). A further increase of annealing temperature from 390 to 430 °C, results in the formation of partially nanochanneled structures from interconnected pores on the nanopyramid arrays by mesopore migration (Figure S31c). Another increase of annealing temperature from 430 to 470 °C results in the formation of "sprouts" of artificial nanofingers from the nanopyramid arrays (Figure S31d). Subsequently, most mesoporous pyramids grow into artificial nanofingers when the annealing temperature increases from 470 to 510 °C (Figure S31e). Finally, as the annealing temperature rises from 510 to 550 °C, an interconnected artificial nanofinger array is formed (Figure S31f). *Ex situ* HRTEM images (Figures S32 and S33) of the artificial nanofingers at different stages indicate the clear structure evolution from mesoporous nanopyramids to nanofingers during the interfacial atomic rearrangement.

2.5. Discussion. Based on the observations above, a thermally induced mesoporous interfacial atomic rearrangement (MIAR) model is proposed for the growth mechanism of ANFs (Figure 5). Different stages of MIAR-growth models with corresponding SEM images (Figure 5a), from small porous pyramids (Stage I), large porous pyramids (Stage II), and pore migration rods (Stage III) to artificial nanofingers (Stage IV) are used to describe the intermediate structures. The detailed analyses of the high-resolution SEM images show that the observed nanofingers are formed from pore migrations in the small domain sizes.

From the microscopic view toward the branching, reorientation and twisting of ANFs, large crystals are formed by the assembly and migration of the polycrystalline small iron oxide domains. As shown in Figure 5b,c, pore migration is observed after thermal treatment from small porous pyramids (Stage I) to large porous pyramids (Stage II), during which small iron oxide domains move and coalesce. Further pore migration is observed from large porous pyramids (Stage II) to nanorods (Stage III), in which the nanorods are formed along

DOI: 10.1021/jacs.5b01747
J. Am. Chem. Soc. 2015, 137, 4260−4266

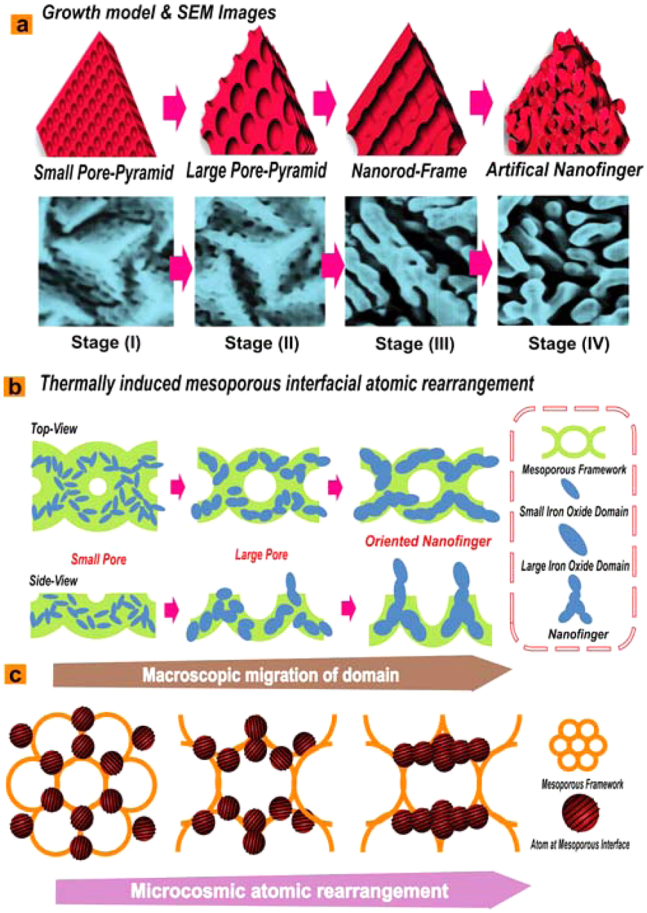

Figure 5. The proposed growth model. (a) Different stages of growth model and corresponding SEM images from small pore pyramids, large pore pyramids, pore migration rods to artificial nanofingers during the atomic interfacial rearrangement process on mesoporous frameworks. (b, c) The proposed thermally induced interfacial atomic rearrangement process, in which the thermal drives branching, reorientation, and twisting from small pore and large pore of mesoporous pyramids to branching artificial nanofingers.

the edges of pyramids and eventually lead to the disappearance of mesoporous frameworks. Further migration and agglomeration of large iron oxide domains on the matrix are clearly observed in SEM images of the artificial nanofingers in stage IV.

The intrinsic surface stresses on mesoporous frameworks result in independent growth of each branched finger.[44,45] The observed nanofingers arise from pore migrations with crystal lattice rearrangement in the small domain sizes, which is considered to be the most important extrinsic factor for the formation of branching nanofinger arrays. The diffraction data of the artificial nanofingers demonstrate high crystallinity as expected, given that nanofingers are well recognized to form uniform, oriented crystals porous interfacial confinement. The asymmetric nanopyramid-directed anisotropic twisting and extending processes are essential for the formation of the branched nanofingers.[46−48] Anisotropic twisting of the mesopore-converted nanorods into branching nanofingers proceeds with self-organization, which tends to form the most stable morphology to release the internal local strain. The atoms on porous frameworks migrate due to the tensile stress, which leads for stress relaxation, which is consistent with the control experiment of Prussian blue nanocubes without substrate confinement. Thus, the branched nanofingers are formed by the combination of mechanical stresses and high diffusion mobility on the mesoporous frameworks.

For the heteroatom-doping approach, the proposed process includes the absorption of guest-doping molecules (Figure S34a) and the subsequent solid−solid interface atom migration (Figure S34b) of mesoporous host-interfaces. During this process, the mesoporous nanopyramids first absorb various guest-doping molecules into the mesopore channels and then convert into heteroatom-doped artificial nanofingers by thermal annealing. To illustrate the effect of Sn-doping on ANFs, the density functional theory (DFT) simulation was carried out.[49−51] The Sn-doped ANFs consists of a relaxed 30-atom hematite unitcell, in which a Sn atom is substituted for a Fe atom (Figure S35a). To investigate the Sn-doping-induced changes in the electronic structure of hematite ANFs, the projected density of states and the total density of states for hematite ANFs of a Sn-doped 30-atom Fe_2O_3 supercell (Figure S35b,c) are plotted. The optimized lattice parameters of pure hematite ANFs are calculated to be a = 5.10 Å and c = 13.75 Å, agreeing closely with previous experimental results (a = 5.04 Å and c = 13.83 Å).[50] For the undoped hematite, the conduction band edge and valence band edge are mostly composed of Fe 3d and O 2p states, respectively. For the Sn-doped system, there is little shift of the position in the conduction and valence band edges, resulting in almost no band gap narrowing, in good agreement with our IPCE results. Sn adopts a D^{4+} oxidation state and creates a charge carrier, resulting in the increase of the charge carrier density. The electrochemical impedance spectroscopy analysis shows that the Nyquist plots of the Sn-doped ANFs have a smaller semicircle diameter than that of the undoped ANFs (Figure S36), suggesting the effectiveness of Sn-doping for improving the charge-transfer properties of hematite.[52] Therefore, both the increases of the charge carrier density and the charge-transfer efficiency lead to the enhanced optoelectronic activity of doped ANFs.

The MIAR method has several advantages. First, it is a unique, versatile doping method that combines the sol−gel process and thermal annealing. The mesoporous frameworks and the solid−solid interface-based thermal annealing enable fast heating and facile assembly for rapid dopant diffusion during the atom migration. Second, this facile MIAR approach allows for simultaneous growth, crystallization, and doping of ANFs, with similar finger-like morphology, orientation, and crystallinity. In addition, the MIAR growth approach can serve as a universal method for doping of various metal ions. Finally, the MIAR growth doping process facilitates the incorporation and optimization of multiple dopants, providing the flexibility of utilizing other dopants as well.

3. CONCLUSION

In summary, we have developed a robust MIAR approach to grow vertical artificial nanofingers, with facile and versatile metal ion doping. The optoelectronic properties of vertical artificial nanofingers can be tailored by different heteroatom dopings enabled by the MIAR method. The Sn-doped ANFs exhibit a high photocurrent density of ~1.26 mA/cm^2 at 0.23 V vs Ag/AgCl, which is ~5.25-fold of the pristine mesoporous Fe_2O_3 nanopyramids and 2.07-fold of the undoped Fe_2O_3 ANFs, respectively. Furthermore, with surface chemical functionalization, the Sn-doped Fe_2O_3 ANFs allow unprecedented nanomolar level capturing and recognition of biomolecules (~5 nm for GSH). The advantage and versatility offered by this approach should have an important impact in

DOI: 10.1021/jacs.5b01747
J. Am. Chem. Soc. 2015, 137, 4260−4266

the synthesis of heteroatom-doped vertical nanostructures with optimized morphology and doping, to fabricate other branched nanoarrays from a variety of mesostructures.

4. EXPERIMENTAL SECTION

4.1. Synthesis of Mesoporous Fe_2O_3 Pyramid Arrays. The Fe_2O_3 pyramids were prepared by the interfacial growth method reported previously in our group.[20] The single-crystalline Prussian blue nanocubes were interfacially grown on a flexible Ti foil, followed by the *in situ* thermal conversion of Prussian blue into Fe_2O_3 pyramids array. In a typical procedure, 136 mg of $K_3[Fe(CN)_6]\cdot 3H_2O$ was first added to 80 mL of hydrochloric acid (0.005 M) under stirring for 30 min. Then, a piece of 2.5 cm × 6.0 cm Ti foil was slowly immersed into the above mixture. After that, the container was placed into an oven and heated at 85 °C for 24 h. The obtained Prussian blue pyramids were taken out from the container, washed with DI water, and finally dried in a vacuum oven at 55 °C for 12 h. To obtain the mesoporous Fe_2O_3 pyramids with various mesopores structures, the as-made Prussian blue pyramids were heated to 350 °C with a temperate ramp of 1 °C min^{-1} for 3 h.

4.2. Synthesis of Heteroatom-Doped Fe_2O_3 ANFs. Heteroatom-doped Fe_2O_3 ANFs were grown on Ti substrates over a broad range of synthesis conditions in terms of different guest molecules, including $SnCl_2$, $Co(NO_3)_2\cdot 6H_2O$, $Ni(NO_3)_2\cdot 6H_2O$, $Cu(NO_3)_2\cdot 3H_2O$, $Zn(NO_3)_2\cdot 6H_2O$, $Bi(NO_3)_2\cdot 5H_2O$, $Na_2WO_4\cdot 2H_2O$, $Cd(NO_3)_2\cdot 4H_2O$, and $MnCl_2\cdot 4H_2O$, to host mesoporous pyramids ratio. Typically, the heteroatom-dopant precursor solution was prepared separately. Then, a piece of 2.5 × 6.0 cm was slowly dipped into the heteroatom-dopant precursor solution (0.005 M, 150 mL) for 24 h and then dried by air blowing. Finally, the heteroatom-doped ANFs were obtained by annealing of heteroatom-dopant precursor-coated nanopyramids in air at 550 °C for 4 h with a heating rate of 1 °C min^{-1}. The surface concentrations of heteroatom-dopants were estimated via a quantitative analysis of ICP-MS.

4.3. Optoelectronic Measurements. The photoelectrochemical measurements were carried out using a transparent three-electrode electrochemical cell, consisting of a modified working electrode, a counter electrode of platinum wire, and a KCl-saturated Ag/AgCl electrode at ambient temperature (~25 °C) under simulated sunlight with a 150 W xenon lamp coupled with an AM 1.5G filter (Newport 94022A).[38,42] The Fe_2O_3 ANFs samples were used as the working electrode with an area about 1 × 2 cm. A phosphate buffer (pH of 7.4) was used as the aqueous background electrolytes for the PEC measurements. Argon bubbling was used to remove oxygen in advance from the solutions in the electrochemical cell. Linear sweeps and amperometry (i–t) scans were measured by a CHI660D electrochemical workstation. The IPCE was collected by a Newport electrochemical station with a solar simulator (Newport 66902, 1000 W xenon lamp), coupled with a filter (Newport 74010), and aligned monochromator (Newport 74125).

4.4. DFT Simulation. DFT calculations were carried out for structural relaxation and electronic structure. The ion–electron interaction was treated by the projector augmented-wave technique,[49] as implemented in the Vienna ab initio simulation package.[50] The exchange–correlation potential was treated using the Perdew–Burke–Ernzerhof functional.[51] The on-site correlation corrections were included using the Hubbard model (DFT + U approach),[53] and the value of the correlation energy (U) was fixed at 5.0 eV for Fe and 4.0 eV for Sn. The k-mesh was generated by the Monkhorst–Pack scheme, where the density of k-points was determined by lattice constant. The antiferromagnetic ground-state ordering was taken, corresponding to a state along [0001] in the hexagonal representation with opposite magnetic moments placed on short distance pairs of Fe atoms and equal magnetic moments on larger distance.[54]

■ ASSOCIATED CONTENT

Supporting Information

Additional SEM, TEM, photograph, nitrogen sorption, EDX, XPS spectroscopic data, and DFT simulation of ANFs are provided. This material is available free of charge via the Internet at http://pubs.acs.org.

■ AUTHOR INFORMATION

Corresponding Authors

*dyzhao@fudan.edu.cn

*gfzheng@fudan.edu.cn

Notes

The authors declare no competing financial interest.

■ ACKNOWLEDGMENTS

This work was supported by the State Key Basic Research Program of the PRC (2012CB224805, 2013CB934104), the NSF of China (20890123, 21322311, and 21473038), the Shanghai Leading Academic Discipline Project (B108), the Science and Technology Commission of Shanghai Municipality (08DZ2270500, 14JC1490500), the Program for Professor of Special Appointment (Eastern Scholar) at Shanghai Institutions of Higher Learning, the Australian Research Council (DP120101194, DP140104062), the Deanship of Scientific Research of King Saud University (IHCRG#14-102).

■ REFERENCES

(1) Oro, J.; Skewes, H. *Nature* **1965**, *207*, 1042.

(2) Meng, F.; Morin, S. A.; Forticaux, A.; Jin, S. *Acc. Chem. Res.* **2013**, *46*, 1616.

(3) Zheng, G.; Patolsky, F.; Cui, Y.; Wang, W. U.; Lieber, C. M. *Nat. Biotechnol.* **2005**, *23*, 1294.

(4) Feng, X.; Shankar, K.; Varghese, O. K.; Paulose, M.; Latempa, T. J.; Grimes, C. A. *Nano Lett.* **2008**, *8*, 3781.

(5) Goldberger, J.; He, R.; Zhang, Y.; Lee, S.; Yan, H.; Choi, H.-J.; Yang, P. *Nature* **2003**, *422*, 599.

(6) Wu, H.; Chan, G.; Choi, J. W.; Yao, Y.; McDowell, M. T.; Lee, S. W.; Jackson, A.; Yang, Y.; Hu, L.; Cui, Y. *Nat. Nanotechnol.* **2012**, *7*, 310.

(7) Peng, H.; Lai, K.; Kong, D.; Meister, S.; Chen, Y.; Qi, X.-L.; Zhang, S.-C.; Shen, Z.-X.; Cui, Y. *Nat. Mater.* **2010**, *9*, 225.

(8) Bai, J.; Cheng, R.; Xiu, F.; Liao, L.; Wang, M.; Shailos, A.; Wang, K. L.; Huang, Y.; Duan, X. *Nat. Nanotechnol.* **2010**, *5*, 655.

(9) Chan, C. K.; Peng, H.; Twesten, R. D.; Jarausch, K.; Zhang, X. F.; Cui, Y. *Nano Lett.* **2007**, *7*, 490.

(10) Zhu, J.; Yu, Z.; Burkhard, G. F.; Hsu, C.-M.; Connor, S. T.; Xu, Y.; Wang, Q.; McGehee, M.; Fan, S.; Cui, Y. *Nano Lett.* **2008**, *9*, 279.

(11) Hsu, C.-M.; Connor, S. T.; Tang, M. X.; Cui, Y. *Appl. Phys. Lett.* **2008**, *93*, 133109.

(12) Jeong, S.; McDowell, M. T.; Cui, Y. *ACS Nano* **2011**, *5*, 5800.

(13) Kong, B.; Tang, J.; Wu, Z.; Selomulya, C.; Wang, H.; Wei, J.; Wang, Y.; Zheng, G.; Zhao, D. *NPG Asia Mater.* **2014**, *6*, e117.

(14) Fan, Z.; Razavi, H.; Do, J.-w.; Moriwaki, A.; Ergen, O.; Chueh, Y.-L.; Leu, P. W.; Ho, J. C. *Nat. Mater.* **2009**, *8*, 648.

(15) Yang, Y.; Xie, C.; Ruffo, R.; Peng, H.; Kim, D. K.; Cui, Y. *Nano Lett.* **2009**, *9*, 4109.

(16) Wu, Y.; Livneh, T.; Zhang, Y. X.; Cheng, G.; Wang, J.; Tang, J.; Moskovits, M.; Stucky, G. D. *Nano Lett.* **2004**, *4*, 2337.

(17) Frindell, K. L.; Bartl, M. H.; Popitsch, A.; Stucky, G. D. *Angew. Chem., Int. Ed.* **2002**, *41*, 959.

(18) Dürr, M.; Schmid, A.; Obermaier, M.; Rosselli, S.; Yasuda, A.; Nelles, G. *Nat. Mater.* **2005**, *4*, 607.

(19) Zhu, J.; Hsu, C.-M.; Yu, Z.; Fan, S.; Cui, Y. *Nano Lett.* **2009**, *10*, 1979.

(20) Kong, B.; Tang, J.; Selomulya, C.; Li, W.; Wei, J.; Fang, Y.; Wang, Y.; Zheng, G.; Zhao, D. *J. Am. Chem. Soc.* **2014**, *136*, 6822.

DOI: 10.1021/jacs.5b01747
J. Am. Chem. Soc. 2015, 137, 4260–4266

(21) Ozel, T.; Bourret, G. R.; Schmucker, A. L.; Brown, K. A.; Mirkin, C. A. *Adv. Mater.* **2013**, *25*, 4515.
(22) Brongersma, M. L.; Cui, Y.; Fan, S. *Nat. Mater.* **2014**, *13*, 451.
(23) Yu, W. J.; Li, Z.; Zhou, H.; Chen, Y.; Wang, Y.; Huang, Y.; Duan, X. *Nat. Mater.* **2013**, *12*, 246.
(24) Jiang, X.; Tian, B.; Xiang, J.; Qian, F.; Zheng, G.; Wang, H.; Mai, L.; Lieber, C. M. *Proc. Natl. Acad. Sci. U.S.A.* **2011**, *108*, 12212.
(25) Wang, D.; Qian, F.; Yang, C.; Zhong, Z.; Lieber, C. M. *Nano Lett.* **2004**, *4*, 871.
(26) Zhu, J.; Peng, H.; Chan, C. K.; Jarausch, K.; Zhang, X. F.; Cui, Y. *Nano Lett.* **2007**, *7*, 1095.
(27) Tian, B.; Kempa, T. J.; Lieber, C. M. *Chem. Soc. Rev.* **2009**, *38* (1), 16.
(28) Bierman, M. J.; Lau, Y. A.; Jin, S. *Nano Lett.* **2007**, *7*, 2907.
(29) Bierman, M. J.; Lau, Y. A.; Kvit, A. V.; Schmitt, A. L.; Jin, S. *Science* **2008**, *320*, 1060−1063.
(30) Zhu, J.; Peng, H.; Marshall, A.; Barnett, D.; Nix, W.; Cui, Y. *Nat. Nanotechnol.* **2008**, *3*, 477.
(31) Lau, Y. A.; Chernak, D. J.; Bierman, M. J.; Jin, S. *J. Am. Chem. Soc.* **2009**, *131*, 16461.
(32) Milliron, D. J.; Hughes, S. M.; Cui, Y.; Manna, L.; Li, J.; Wang, L.-W.; Alivisatos, A. P. *Nature* **2004**, *430*, 190.
(33) Manna, L.; Scher, E. C.; Alivisatos, A. P. *J. Am. Chem. Soc.* **2000**, *122*, 12700.
(34) Liu, B.; Aydil, E. S. *J. Am. Chem. Soc.* **2009**, *131*, 3985.
(35) Kong, B.; Tang, J.; Wu, Z.; Wei, J.; Wu, H.; Wang, Y.; Zheng, G.; Zhao, D. *Angew. Chem., Int. Ed.* **2014**, *53*, 2888−2892.
(36) Lu, A.-H.; Nitz, J.-J.; Comotti, M.; Weidenthaler, C.; Schlichte, K.; Lehmann, C. W.; Terasaki, O.; Schuth, F. *J. Am. Chem. Soc.* **2010**, *132*, 14152.
(37) Deng, Y.; Wei, J.; Sun, Z.; Zhao, D. *Chem. Soc. Rev.* **2013**, *42*, 4054.
(38) Tang, J.; Zhang, Y.; Kong, B.; Wang, Y.; Da, P.; Li, J.; Elzatahry, A. A.; Zhao, D.; Gong, X.; Zheng, G. *Nano Lett.* **2014**, *14*, 2702.
(39) Ling, Y.; Wang, G.; Wheeler, D. A.; Zhang, J. Z.; Li, Y. *Nano Lett.* **2011**, *11*, 2119.
(40) Tang, J.; Kong, B.; Wang, Y.; Xu, M.; Wang, Y.; Wu, H.; Zheng, G. *Nano Lett.* **2013**, *13*, 5350.
(41) Tian, B.; Liu, J.; Dvir, T.; Jin, L.; Tsui, J. H.; Qing, Q.; Suo, Z.; Langer, R.; Kohane, D. S.; Lieber, C. M. *Nat. Mater.* **2012**, *11*, 986.
(42) Tang, J.; Kong, B.; Wu, H.; Xu, M.; Wang, Y.; Wang, Y.; Zhao, D.; Zheng, G. *Adv. Mater.* **2013**, *25*, 6569.
(43) Zhang, F.; Wen, M.; Cheng, M.; Liu, D.; Zhu, A.; Tian, Y. *Chem.—Eur. J.* **2010**, *16*, 11115.
(44) Toda, A.; Taguchi, K.; Kajioka, H. *Macromolecules* **2008**, *41*, 7505.
(45) Bets, K. V.; Yakobson, B. I. *Nano Res.* **2009**, *2*, 161.
(46) Hu, B.; Shi, W.; Wu, Y. L.; Leow, W. R.; Cai, P.; Li, S.; Chen, X. *Adv. Mater.* **2014**, *26*, 5786.
(47) Zhang, D.-B.; Dumitrică, T. *Phys. Rev. B* **2010**, *82*, 193401.
(48) Zhao, M.-Q.; Zhang, Q.; Tian, G.-L.; Huang, J.-Q.; Wei, F. *ACS Nano* **2012**, *6*, 4520.
(49) Blöchl, P. E. *Phys. Rev. B* **1994**, *50*, 17953.
(50) Kresse, G.; Hafner, J. *Phys. Rev. B* **1994**, *49*, 14251.
(51) Perdew, J. P.; Burke, K.; Ernzerhof, M. *Phys. Rev. Lett.* **1996**, *77*, 3865.
(52) Wang, X.; Liow, C.; Qi, D.; Zhu, B.; Leow, W. R.; Wang, H.; Xue, C.; Chen, X.; Li, S. *Adv. Mater.* **2014**, *26*, 3506.
(53) Anisimov, V. I.; Aryasetiawan, F.; Lichtenstein, A. *J. Phys: Condens. Matter.* **1997**, *9*, 767.
(54) Rollmann, G.; Rohrbach, A.; Entel, P.; Hafner, J. *Phys. Rev. B* **2004**, *69*, 165107.

DOI: 10.1021/jacs.5b01747
J. Am. Chem. Soc. 2015, 137, 4260−4266